Operando Monitoring of the Solution-Mediated Discharge and Charge Processes in a Na–O 2 Battery Using Liquid-Electrochemical Transmission Electron Microscopy

Lukas Lutz, Walid Dachraoui, Arnaud Demortière, Lee R Johnson, Peter Bruce, Alexis Grimaud, Jean-marie Tarascon

Operando monitoring of the solution-mediated discharge and charge processes in a Na-O_2 battery using liquid-electrochemical TEM

Lukas Lutz[1,3,4], Walid Dachraoui[2,3], Arnaud Demortière[2,3]*, Lee R. Johnson[4], Peter G. Bruce[4], Alexis Grimaud[1,3]*, and Jean-Marie Tarascon[1,3]

[1] Collège de France, 11 Place Marcelin Berthelot, 75231 Paris, France

[2]Laboratoire de Réactivité et Chimie des Solides (LRCS), CNRS UMR 7314, 80009 Amiens, France

[3]Réseau sur le Stockage Electrochimique de l'Energie (RS2E), FR CNRS 3459, France

[4]Department of Materials, University of Oxford, Parks Road, Oxford OX1 3PH, UK

Corresponding authors: Alexis Grimaud <alexis.grimaud@college-de-france.fr>, Arnaud Demortière <arnaud.demortiere@energie-rs2e.com>

Abstract

Despite the fact that in sodium-oxygen (Na-O_2) batteries show promise as high-energy storage systems, this technology is still the subject of intense fundamental research, owing to the complex reaction by which it operates. To understand the formation mechanism of the discharge product, sodium superoxide (NaO_2), advanced experimental tools must be developed. Here we present for the first time the use of a Na-O_2 micro-battery using a liquid aprotic electrolyte coupled with fast imaging transmission electron microscopy to visualize, in real time, the mechanism of NaO_2 nucleation/growth. We observe that the formation of NaO_2 cubes during reduction occurs by a solution-mediated nucleation process. Furthermore, we unambiguously demonstrate that the subsequent oxidation of NaO_2, of which little is known, also proceeds via a solution mechanism. We also provide insight into the cell electrochemistry via the visualization of an outer shell of parasitic reaction product, formed through chemical reaction at the interface between the growing NaO_2 cubes and the electrolyte, and suggest that this process is responsible for the poor cyclability of Na-O_2 batteries. The assessment of the discharge- charge mechanistic in Na-O_2 batteries through *operando* electrochemical TEM visualization should facilitate the development of this battery technology.

Keywords: Na-O_2 battery, solution-mediated mechanism, discharge and charge processes, Operando TEM, Parasitic product formation

Introduction

Compared to Li/Na-ion batteries, in which reversible energy storage relies on the use of redox active transition metal oxides as positive electrodes, the metal-O_2 battery systems would theoretically offer greater energy density owing to the use the redox of gaseous oxygen using conductive and light carbon electrodes.[1, 2] The aprotic lithium-oxygen (Li-O_2) system has been widely studied since the early demonstration of reversibility by K.M. Abraham.[3] Nevertheless, recent developments clearly pointed out towards drastic limitations in terms of round trip efficiency as well as coulombic efficiency due to copious parasitic reactions of the discharge product lithium peroxide (Li_2O_2) with both the conductive electrode and the electrolyte. [4-6]Following this conclusion, the sodium-oxygen (Na-O_2) system was then proposed as a viable alternative due to its theoretical energy density of 1100 Wh/kg combined with a better round trip efficiency and presumably limited parasitic reactions.[7] The Na-O_2 system is still, however, in its infancy, owing to several unresolved challenges, such as limited capacities and low cyclability.[8, 9] Hence, the initial excitement was quickly counterpoised by the recent discoveries highlighting the unstable nature of the superoxide discharge product sodium superoxide (NaO_2) that reacts with glyme-ethers solvent commonly used in these systems. Despite these evident limitations, this system has been seen as an interesting case study to better understand the complex redox reaction of oxygen in aprotic solvent that involves a gas to solid phase transformation. Only mastering these complex transformations will eventually trigger the development of rechargeable metal-O_2 batteries and deliver the initial promises offered by the large energy density for these systems.

Further efforts are thus required to understand and master the formation and decomposition processes of the micron-sized cubic NaO_2 product, which is at the core of the Na-O_2 electrochemistry and still under heavy debate. Contradictory results discussing either a solution-mediated discharge and charge reaction, the need for phase transfer catalysts (e.g.:

H_2O) that increases the solubility of NaO_2, or an electrode-surface directed mechanism, leave the question for the fundamental reaction path unanswered.[5, 10-17] One reason for that is surely the high sensitivity of the NaO_2 product and its reactivity towards moisture[18, 19], CO_2[20, 21] and other electrolyte impurities, which makes any analysis by *ex situ* methods extremely difficult. This also explains the absence of a common consensus regarding the parameters controlling the formation of NaO_2 as well as the underpinning mechanism for NaO_2 decomposition. [5, 10-17]

Another challenge of the Na-O_2 system is associated to its unsatisfactory cyclability, where recent papers have demonstrated that the fast death of the battery, after only few cycles, is associated to the low stability of the NaO_2 discharge product.[8, 22] Others further identified the detrimental ability of NaO_2 to trigger parasitic reactions, where the origin of the parasitic reactions includes the oxidation of the electrolyte and the carbon electrode, consequently forming side products such as carbonates, carboxylates, formates and acetates.[8, 23-25] However, such results were obtained *ex situ*, hence leaving questions concerning the underpinning mechanism or the effect of post-mortem sample handling, open.

Altogether, these studies clearly demonstrate the complexity of the Na-O_2 system, which have slowed down its development. Thus, there is a need to move away from the conventional analytical *ex situ* characterization methods and develop *operando* techniques to pin-down fundamental mechanisms in real-time.[26] The recent development of liquid cell for transmission electron microscopy[27] enables an exciting opportunity to explore[28, 29] and even quantify[30-32] complex electrochemical reactions occurring inside batteries during operation. In the present study, we monitor for the first time the discharge and charge reactions occurring in a liquid aprotic Na-O_2 battery by using an *operando* electrochemical (scanning) transmission electron microscopy (STEM and TEM) Na-O_2 micro battery setup coupled with fast imaging. This setup enables us to unambiguously prove that not only does the growth occur by a solution-mediated processes in glyme-ether electrolytes, but so does the oxidation of NaO_2

cubes. Further, we visualize the formation of side products leading to the formation of parasitic shell at the interface between NaO_2 crystals and the electrolyte, which remains as solid residues on the electrode after charge.

Benchmarking the Na-O_2 micro-battery setup

Figure 1 shows a schematic of the micro-battery based on the electrochemical TEM cell configuration (a-d) used throughout this work for the *operando* imaging of sub-micrometric features during redox reactions at the positive carbon electrode (e). The *operando* cell was assembled using an oxygen-saturated electrolyte made of 0.5M $NaPF_6$ dissolved into monoglyme (DME), which contains < 20 ppm of water as determined by Karl-Fischer titration. To establish its electrochemical performance, the *operando* cell was charged and discharged in a cyclic-voltammetry mode, using a sweep rate of 10 mV/s between and Pt as counter and pseudo-reference electrodes (Supplementary Figure S1). Such conditions were used due to the extremely small size of the cell setup, restricting the volume of the electrolyte as well as the available amount of dissolved O_2. We first verified that these conditions provide similar results as classical Swagelok cells, with namely the formation of discharge products consisting of plentiful cubes (Figure 2a and 2b), which were identified as NaO_2 by combining energy dispersive X-ray spectroscopy (EDX) and selected area electron diffraction (SAED) as discussed later in greater detail.

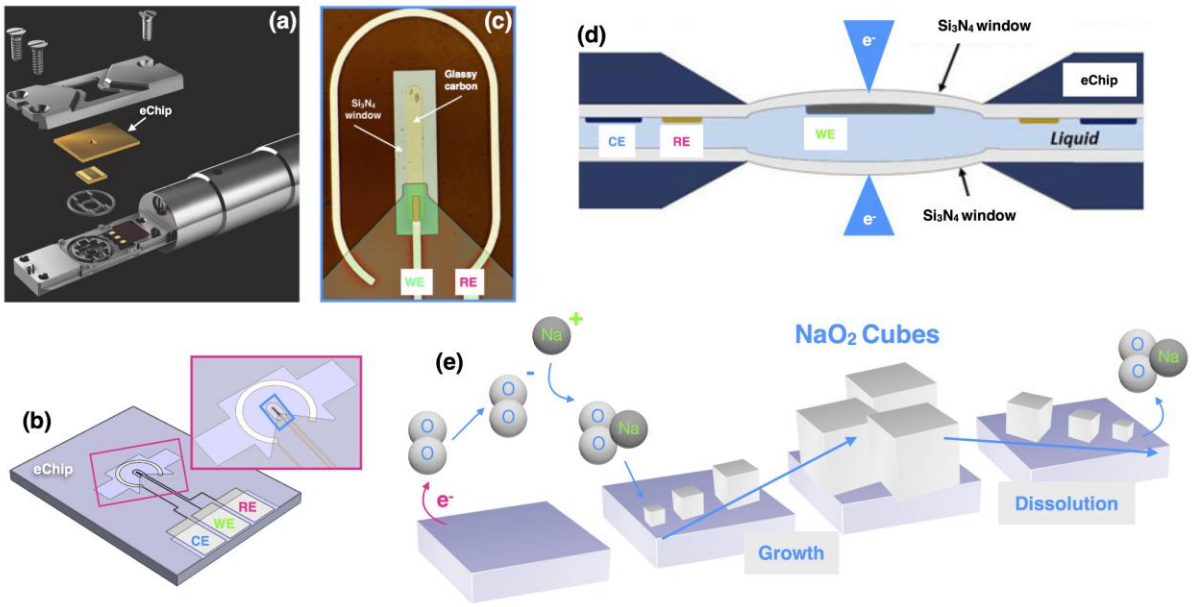

Figure 1: Schematic description of the Poseidon 510 TEM holder for *operando* electrochemical measurements: exploded view showing the holder tip with precision slot for loading liquid cell (a), where the top e-chip containing a printed reference (platinum), counter (platinum) and working electrode (glassy carbon) (b, c) is mounted on top of the bottom e-chip containing an electron beam transparent Si_3N_4 membrane, O-rings gasket is used to get a good vacuum-sealing. Cross-sectional illustration of the *operando* electrochemical TEM cell with the pathway of the electron beam and thin conductive glassy carbon electrode (d). Schematic of the electrochemically induced discharge and charge processes, taking place at the positive electrode surface (e).

Equally, the inhomogeneous dispersion in size and morphology for the cubes obtained on the glassy carbon electrode (GC) in the *operando* cell (loaded with liquid electrolyte) Figure 2d - f, compares well with NaO_2 cubes found in Swagelok-cells on carbon fibers (Figure 2a and 2f).[33, 34] Nevertheless, smaller NaO_2 cubes are formed with the *operando* TEM cell (0.5 - 1 µm) that is explained by the geometry of the cell, *i.e.* the reduced distance between the two

135 Si_3N_4 windows, which limits the amount of electrolyte and thus O_2, as well as the short
136 discharge period during CV.

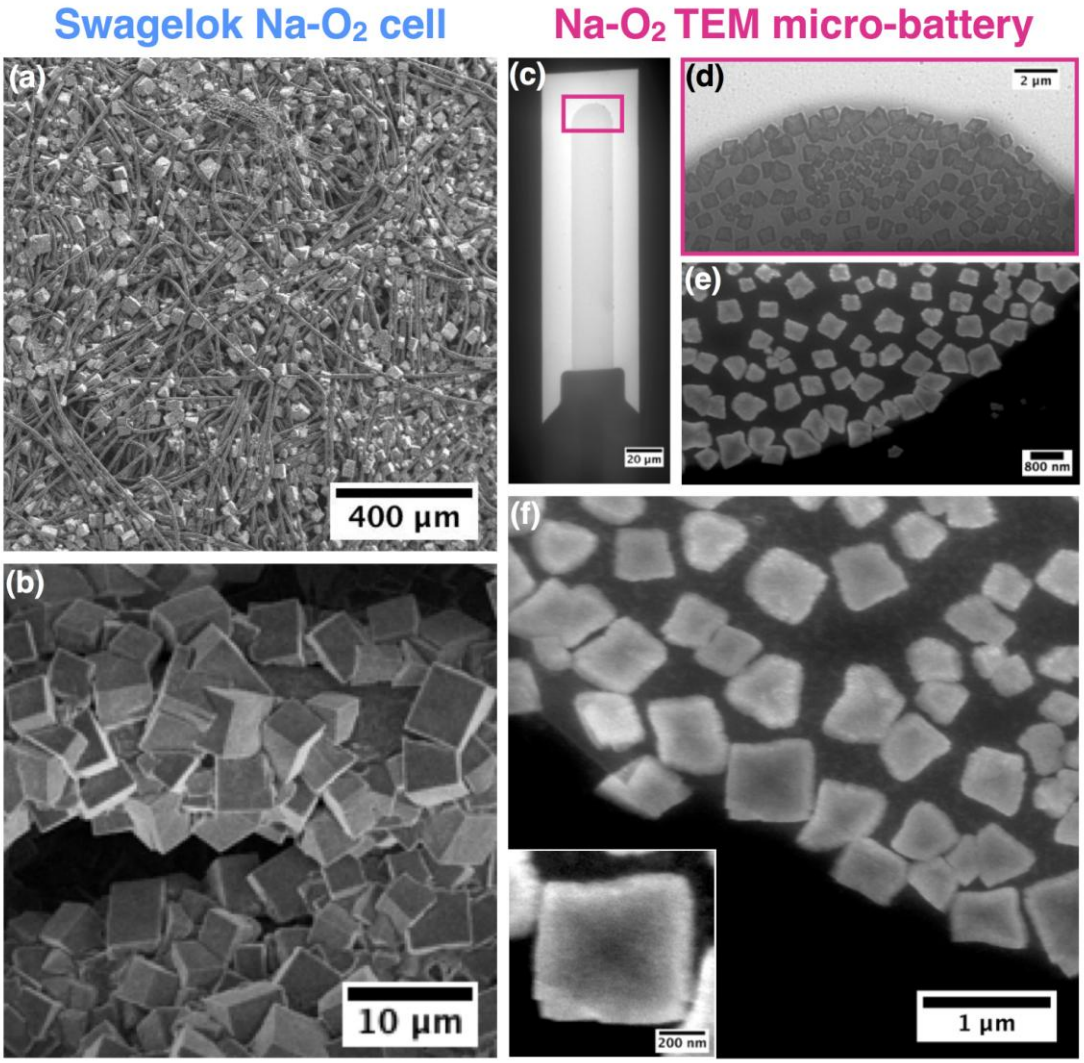

137

138 **Figure 2:** Comparison of Na-O_2 morphology obtained in regular Na-O_2 Swagelok cells on
139 carbon fibers (Freudenberg gas diffusion layer electrodes) (a-b) and the GC electrodes used in
140 the Na-O_2 TEM micro-battery setup (c-f), (images a-d, taken after removal of the electrolyte).
141 The SEM overview image of the carbon fibers shows the dense coverage by NaO_2 discharge
142 product (a) and the high magnification SEM image depicts the micrometer-sized cubic
143 morphology found in Swagelok cells (b). Low magnification TEM image of the GC working
144 electrode used in the *in situ* Na-O_2 micro-battery cell (c). TEM and HAADF-STEM overview
145 images in presence of liquid electrolyte showing, similar to Swagelok cells, NaO_2 cubes

covering the GC electrode after discharge (anodic CV scan, 10 mV/s) (d, e). The enlarged HAADF-STEM images illustrate the inhomogeneous NaO_2 cubes morphology (f and insert); where the thick layer of liquid electrolyte about 1 µm between the electrode surface and the bottom silicon nitride window impacts the image quality even in HAADF-STEM mode.

Visualizing the growth process of NaO_2 during discharge

The growth of NaO_2 cubes during discharge was followed by means of fast TEM imagining and high angle annular dark field STEM (HAADF-STEM) using the same cycling conditions as previously mentioned (Figure 3, sequence a and e, Supplementary Video S1). Comparing the electrochemical response in Figure 3 c with the image sequence in Figure 3 a shows that the cube growth follows a solution-precipitation mechanism. Indeed, after an initial step where the electrolyte is saturated by the electrochemically produced NaO_2 soluble species (image at 5 s, cathodic current in CV of Figure S1), a point of super saturation is then reached as characterized by the formation of small NaO_2 nuclei on the electrode surface (image at 10 s). This initial incubation period, where cathodic current corresponding to the electrochemical formation of soluble NaO_2 is measured but no product is formed on the electrode, is characteristic of a crystal growth following a solution-precipitation mechanism and therefore rules out a surface-directed growth of NaO_2 cubes, for which NaO_2 would grow as a solid following the cathodic current. Such nuclei subsequently grow in an isotropic manner (images at 15 - 60 s), by deposition of solvated NaO_2 on the surface of cubes. This growth ultimately leads to the formation of NaO_2 cubes with a size of approx. 500 nm (image at 60 s). Hence, three stages for the solution-mediated cube-growth precipitation process, similar to the first description given by Janek and coworkers,[15] could be spotted. First, soluble NaO_2 is electrochemically formed and quickly saturate the electrolyte (owing from the low solubility

of NaO_2 in organic solvents)[15, 34]. Once supersaturation of the electrolyte is reached, small aggregates of solvated $(NaO_2)_n$ species precipitate in the form of small NaO_2 nuclei on the carbon electrode. Finally, upon discharge, soluble NaO_2 species are consistently produced and deposit on the high surface energy nuclei, which ultimately grow into larger NaO_2 cubes. We would like to emphasize here is that the electrode surface in Figure 3 sequence a and e, is hard to visualize owing to the thick layer of electrolyte between the electrode and the Si_3N_4 window. Hence, to facilitate its identification, a thin white line is used, as a guide to the reader, to indicate the electrode border in TEM image in Figure 3 b.

Further exploiting the capability of the TEM setup, we visualize the sequential size evolution of several cubes (Figure 3 b, supplementary Video S2). As NaO_2 is an insulator[15, 16] and cannot grow by electrodeposition, it is evident that the gradual growth occurs by deposition of NaO_2 from the solution at the outer crystal surface. For better quantification, the particle size evolution during discharge as a function of the growth time was plotted, which revealed the non-linear intermittent growth rate (Figure 3 c). Initially, the electrolyte is being saturated with electrochemically generated NaO_2 and no significant deposit can be observed. Once the saturation limit is reached, a rapid increase of the cube size is observed, which could be associated with the large concentration of $NaO_{2(solv)}$ in solution at the point of super saturation. This initial burst is then followed by step-wise regime associated with domains of low and high growth rates, dependent on the local concentration of NaO_2 in solution. Lastly, a steady-state regime is reached towards the end of discharge where the growth rate diminishes due to depletion of O_2 in the electrolyte, causing the limited current density as recorded by CV (Figure 3 c). By analyzing several cubes, we could demonstrate that the overall mechanism is similar for every cube, verifying the ubiquitous nature of this process with, however, different intermittent growth rates for each cube, thus further pointing out the

important role played by the mass transport, owing to the different local environment (*i.e.* the density of neighboring cubes) (Figure 3 c). To the best of our knowledge, this is the first acquisition of such insights regarding the solution-mediated growth of NaO_2. These results, combined with the previously demonstrated solubility of NaO_2[15, 34] unambiguously establish that the insulating NaO_2 phase[15, 16] formed during discharge of a Na-O_2 battery is the consequence of a solution-mediated precipitation process.

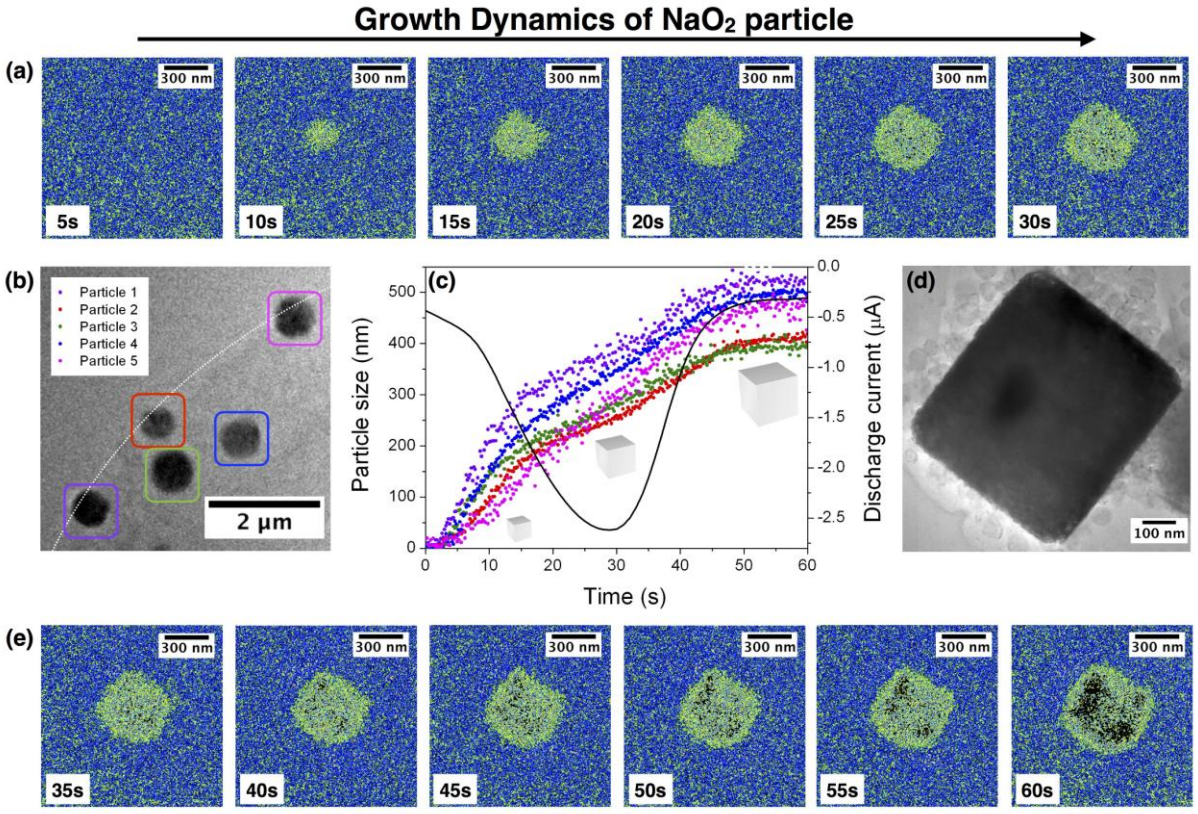

Figure 3: The time-resolved and animated *operando* TEM images illustrate the morphological evolution of the NaO_2 product during discharge (a and e), featuring a nucleation event (10 s) and the subsequent growth of NaO_2 cubes, following a solution-mediated growth-process (11-60 s). TEM image extracted from the growth study of several cubes (pink, blue, green, red and black circles in b) forming during discharge. The size-evolution analysis of these cubes reveals a non-linear growth with intermittent plateaus demonstrating the $NaO_{2(solv)}$ diffusion dependency of this process (c). The black line indicates

the anodic current response obtained during discharge. Enlarged TEM image of a cube obtained at the end of discharge, surrounded by parasitic shell. (d) High-resolution TEM image of NaO_2 cube, obtained on the GC electrode at the end of discharge.

Formation of parasitic shell

Quite interestingly, the use of *operando* TEM also enables identification of a shell surrounding the NaO_2 cubes, which becomes predominant towards the end of discharge (> 60s) (Figure 4 a, image 65 s – 85s, green and orange pixels). We further exploited the capabilities of operando TEM by visualizing the evolution of this shell surrounding the cubic NaO_2 crystal (Supplementary Video S3), shell which is initially appears as a thin film prior to develop into a thick spherical shell (approx. 200 nm) around the cube. Hence, several questions arise from this observation: what is the nature of this shell and what is its consequence for the performance of the Na-O_2 battery?

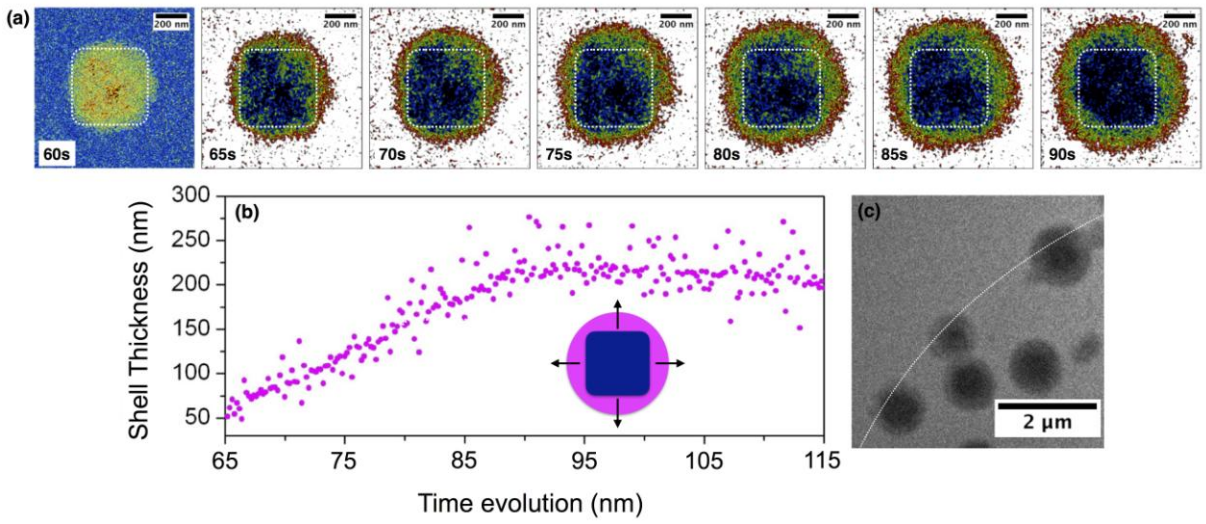

Figure 4: The fast and animated *operando* TEM images showing the evolution of the parasitic shell at the cube-electrolyte interface, illustrated by the orange/green pixels (a). Shell thickness evolution, extracted from the numerical treatment of image stack after contrast filtering, indicated in pink, insert (b). TEM image of finally obtained NaO_2 cubes (strong

contrast), surrounded by the parasitic shell (light contrast) (c). Note that cubes are growing on the surface of the glassy carbon electrode, the extremity of which is represented by the white line.

Analyzing the discharge products

By moving to *ex situ* TEM, EDX and SAED analysis, we could provide further insights in both the chemical composition and the morphology of this shell (Figure 5). Note that this shell, which is separated from crystalline NaO_2 cube by a darker line (in the HAADF-STEM mode), can be found on the surface of every cube (Figure 5 a). Furthermore, the use of TEM reveals the presence of three different morphologies and chemical compositions from the bulk to the surface of a cube (Figure 5 b). First, the bulk crystal (green/blue area) was identified to have the composition of Na:O_2 by means of EDX and to crystallize in the fluorite structure of NaO_2 (S.G. Fm-3m) as deduced by SAED (Figure 5 c, e). Moving towards the surface, TEM reveals a first shell growing on the bulk NaO_2 crystal (pink area), which consists of an agglomeration of nano-cubes with crystallite size of about 20 nm. The SAED pattern of the nano-cubes (Figure 5 f) shows rings of modulated intensity confirming the visual observation of numerous randomly oriented crystallites, having a cubic unit cell parameter close to that measured for the SAED pattern of NaO_2. Although the absolute values for the lattice parameters cannot be precisely measured from SAED patterns, their ratio can be estimated with much higher precision. This estimate gives the $a_{\text{nano-cubes}}/a_{\text{NaO2}} \approx 1.015$ value. Both, the fluorite-type NaO_2 and antifluorite-type Na_2O both possess the face-centered cubic unit cell with the cell parameter ratio $a_{\text{Na2O}}/a_{\text{NaO2}}$ = 5.56Å/5.512Å = 1.009 that is reminiscent to the experimentally measured ratio. Thus, one can tentatively identify the nano-cubes as defective NaO_2, with an increased Na:O atomic ratio (note that Na_2O_2 would adopt an hexagonal

symmetry while $Na_2O_2.2H_2O$ would adopt a monoclinic symmetry). These high surface area cubes may further favor the chemical reactivity towards electrolyte decomposition as seen by the formation of the third shell, an amorphous layer at the outer surface, *i.e.* at the interface between the cubes and the electrolyte, with reduced Na content as deduced by the small sodium peak observed by EDX analysis (Figure 5 d, blue line). To shine further light on this amorphous outer layer, GDL electrodes were discharged using classical Swagelok cells. The electrodes, which contain large amounts of discharge product, were then analyzed in greater details.

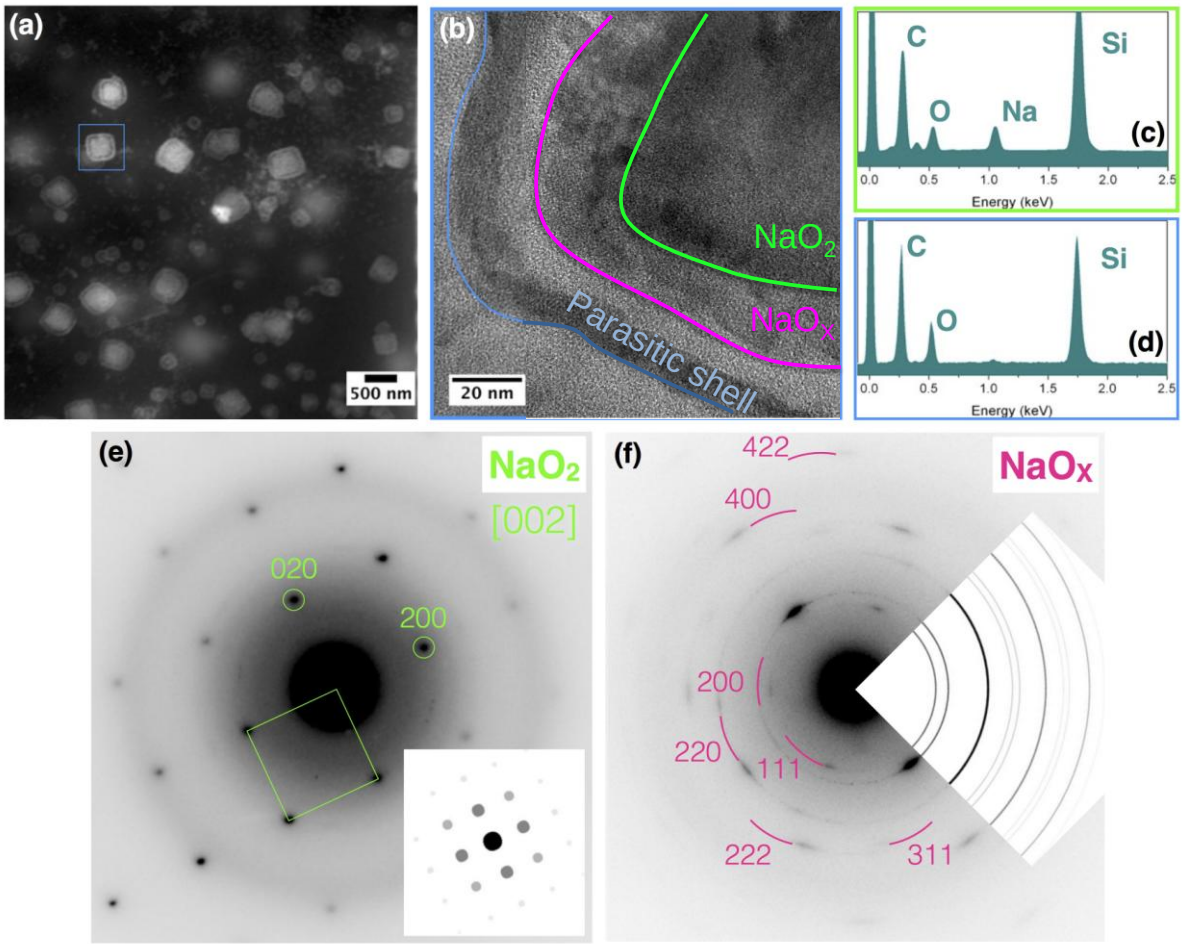

Figure 5: *Ex situ* analysis (dry condition) of the discharge product. HAADF-STEM overview image of the widely distributed cubes on the GC electrode, surrounded by the parasitic shell

(a). TEM image illustrating the interior of the shell around the NaO_2 cubes; bulk crystalline NaO_2 (green), NaO_x nanocrystalites (pink) and the outer organic layer (blue) (b). EDX spectra of the NaO_2 bulk (c) and the organic layer (d). SAED patterns showing the high crystallinity of inner NaO_2 bulk (e) and poly-dispersed NaO_x nanocrystallites for the second layer (f).

First, HAADF-STEM analysis of discharged GDL electrodes revealed the presence of a shell for NaO_2 cubes grown in classical Swagelok cells, similarly to what was observed using the in situ TEM setup (Supplementary Figure S6). This validates the observations made by the operando-cell and further exclude beam damage as the sole origin for the formation of this shell.

To gain deeper understanding about this shell, XPS spectra of discharged GDL electrodes were collected at various stages of discharge (Supplementary Figure S2). The C1s spectra reveal the constant evolution of a parasitic carbonate-like species during discharge. To quantify the amount of these carbonates generated upon discharge, we relied on the method first described by Thotiyl et al.[35] that consist in the use of acid (H_3PO_4) and Fentons`s reagent are used to decompose inorganic and organic carbonates, with the CO_2 generated through their decomposition being subsequently sampled by a mass spectrometer.

The released CO_2 concentration at various stages of discharge (Figure 6) indirectly, demonstrates the significant amount of inorganic Na_2CO_3 and organic carboxylates formed on the surface of carbon electrodes. Upon discharge, the concentration of inorganic carbonates significantly increases (Figure 6 b), and this is in agreement with the growth of the shell observed in Figure 4a. Moreover, when comparing the concentration of Na_2CO_3 at the end of discharge with the results obtained at the end of charge, a limited increase is found for GDL electrodes, demonstrating that the parasitic products cannot be reoxidized and remain on the

electrode surface at the end of charge (Figure 6b). This result highlights the importance of mastering this interface for decreasing the rate of parasitic product formation.

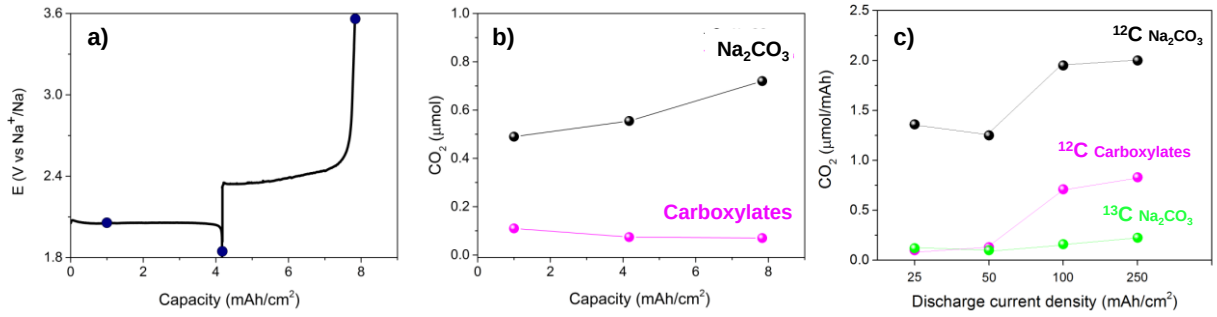

Figure 6: Discharge−charge profiles for GDL electrode at a rate of 25 µA/cm^2 (a). Amount of CO_2 evolved from the GDL electrode when removed from the cells at different states of discharge and charge and treated with acid and Fenton's reagent to decompose Na_2CO_3 and organic carboxylates (b). CO_2 evolution originating from the instability of electrode and electrolyte as deduced from the discharge of ^{13}C-carbon electrodes at various discharge rates between 25 – 250 uA/cm^2 (c). $^{12}CO_2$ evolution indicates the electrolyte degradation leading to inorganic carbonates (black) and organic carboxylates (red) whereas $^{13}CO_2$ detection results from the direct decomposition of the carbon electrodes.

Finally, to clarify the origin of the carbonate side product formation, which can result from the electrolyte and/or from the electrode decomposition, discharge experiments using ^{13}C-labeled electrodes with the released CO_2 isotopes being detected by mass Spectrometry analysis. These isotopic experiments revealed the presence of both $^{13}CO_2$ and $^{12}CO_2$ at the end of discharge, which can only be explained by the decomposition of both the electrode surface and the electrolyte, respectively (Figure 6c). However, the observed ^{12}C fraction was much larger than the ^{13}C one, demonstrating that the majority of parasitic carbonates originates from

the instability of the glyme-electrolyte in contact with the highly oxidizing NaO_2 discharge product. Again, this result corroborates the shell formation we observed in Figure 4. Additionally, we observed that upon elevated discharge currents, the amount of products originating from the decomposition reactions increases, with a prominent contribution from the electrode decomposition (Figure 6c), hence implying that an electrochemically-driven-electrode decomposition is also at play during discharge of Na-O_2 batteries.

Altogether, these experiments reveal the high reactivity of NaO_2 and further disproves, together with previous literature reports, [8, 23-25] the initial claim of improved stability for Na-O_2 batteries when compared to Li-O_2 ones.[5]

Overall, the combination of the time-resolved TEM as well as *ex situ* observations reveal that parasitic reactions in glyme-ether based Na-O_2 batteries constantly occur during discharge, demonstrating the strong reactivity of NaO_2 towards the electrolyte and potentially residual impurities such as *e.g.*: H_2O or CO_2 [18, 20, 21] or even the generation of singlet O_2 species, as recently reported for Li-O_2 and Na-O_2 batteries.[36-38] At this stage, it is worth noting that the carbonates are certainly not the only one kind of parasitic products formed when cycling Na-O_2 batteries. Indeed, several very recent reports demonstrated the high reactivity of NaO_2 towards the electrode, as well as towards the solvent,[8, 23, 24] where sodium carbonate and carboxylate were identified to be the main parasitic products, with a variety of other side products, such as formats and acetates also being found.

Overall, we believe that preventing the formation of this complex organic/inorganic shell will be of prime importance to mitigate the drastic capacity loss observed upon cycling with todays' Na-O_2 cells, which will be discussed in greater details below.

Resolving the mechanism in charge – the dissolution of NaO_2

Encouraged by the mechanistic insight provided by *operando* TEM during the discharge of Na-O_2 battery, we decided to explore the oxidation process following the same methodology. From a sequence of images collected by HAADF-STEM (Supplementary Video S4), the gradual dissolution of NaO_2 cubes during oxidation can be observed (Figure 7). More importantly, this visualization shows that cubes dissolve concentrically from the outside inwards. In detail, the 3D visualization of the processes at play during charge illustrate that the dissolution of the cubes initially proceeds from the top surface, *i.e.* at the interface between the cube and the electrolyte, leading to a steady decrease in size of the cube (Figure 7 a-d). This is in contrast to the previously reported electrode directed charge-transfer, *i.e.* the direct oxidation of the cubes at the interface with the electrode.[12] To gain deeper insight into this dissolution process, the height-profile evolution was followed for one cube throughout the complete oxidation (Figure 7 e-h). From this profile, it can be observed that cubes, despite being covered by the parasitic shell, start to dissolve from the top, *i.e.* the face exposed to the electrolyte, hence demonstrating the porous nature of the organic shell. Upon further charging, the overall height profile continuously decreases from the top of the cube, further suggesting a collapse of the parasitic shell during charge. Ultimately, parts of the shell remain at the end of charge spread on the surface of the electrode, visualized in Figure 7 i as a patchwork and by the "walls" at 50 and 300 nm in the linear profile in Figure 7 h. This is in good agreement with our *ex situ* observations where parasitic residues (organic and inorganic) are found on the GDL carbon fibers after charge (Figure 6), as well as with previous reports.[8] Altogether, these new information shine light on a so-far poorly explained phenomenon, namely the constant columbic losses measured upon cycling. Subsequent cycling will indeed generate additional parasitic products that will accumulate at the electrode surface, ultimately causing a rapid capacity loss and a drastic self-discharge.

In light of the solvation-desolvation equilibrium discussed above, our *operando* electron microscopy measurements provide the definitive demonstration that the oxidation process in Na-O_2 batteries follows a solution-mediated mechanism, as previously proposed[15] based on the significant solubility of NaO_2,[15, 34] its low dissolution energy[10, 13] as well as its insulating nature that would prohibit direct oxidation at the electrode.[15, 16] During charge, solvated $NaO_{2(solv)}$ is oxidized at the electrode surface into Na^+ and $O_{2(g)}$, hence displacing the equilibrium $NaO_{2(solid)}$ = $NaO_{2(solv)}$ to the right and forcing the dissolution of the cubes. Through this process, the bottom edges of the non-conducting cubes, in direct contact with the electrode surface, remain throughout the charge as evidenced by TEM. This clearly contrasts with the previously proposed mechanism for which a direct charge transfer between the solid and the electrode/current collector was a requirement.[12]

Finally, we explored the consequences of the formation of parasitic products at the electrode surface on subsequent cycles and NaO_2 formation. This revealed that NaO_2 nuclei were exclusively formed during the second discharge on the uncovered, pristine electrode surface (Supplementary Video S5). Hence, the parasitic products not only hamper the $O_{2(g)}$ redox reaction but also hinder NaO_2 nucleation on the carbon surface. In short, this study shows that the formation of parasitic products has its origin in the high chemical reactivity of the NaO_2 cube surface, initially suspected to be less reactive than Li_2O_2.[5] This highlights the need for a new class of electrolytes that are stable against attack from NaO_2.

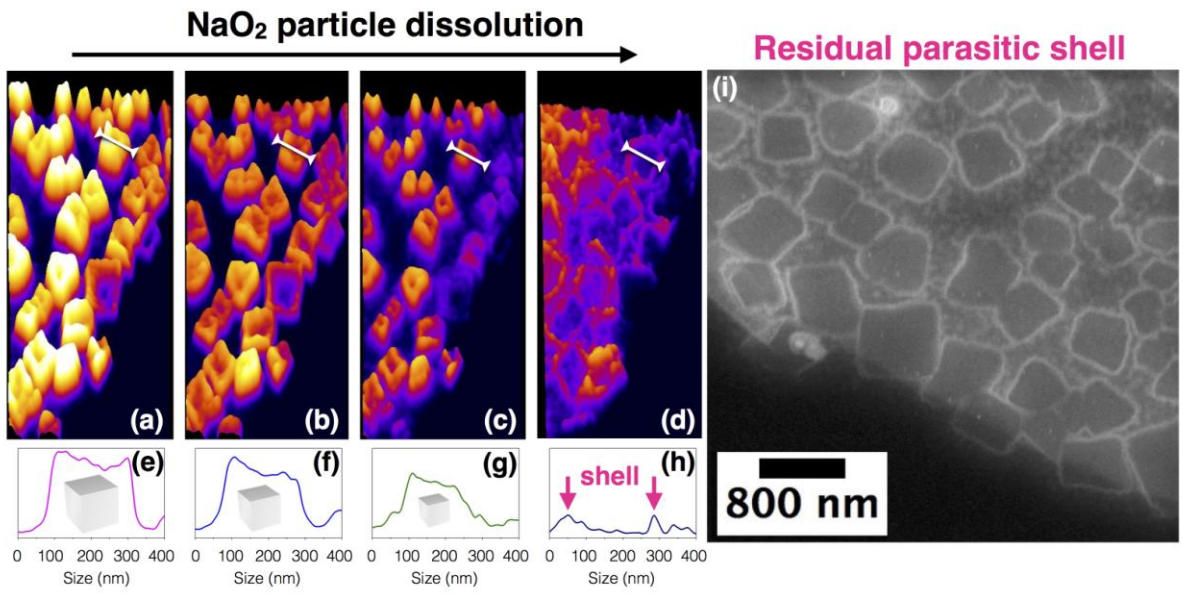

Figure 7: HAADF-STEM imaging of the charge process. Animated images at different depth of charge depict the dissolution of the cubes via solution, starting at cube-electrolyte interface and proceeding downwards to the electrode surface (a-d). High profile evolution of a single cube during charge (specified by white bar in a-d) (e-h) further supporting the solution-mediated charge, where the two bumps at 50 and 300 nm in image h indicate the parasitic shell remaining on the electrode surface at the end of the charge. HAADF-STEM image of the GC electrode surface after discharge showing the patchwork of the residual parasitic shells, blocking subsequent O_2 redox and NaO_2 nucleation (i).

Conclusion

Herein we have reported that fast imagining TEM and HAADF-STEM are powerful analytical tools to understand the mechanistic pertaining to the charge/discharge processes in DME based Na-O_2 batteries. We visualized the solution-mediated growth of NaO_2 in real-time and identified that the 3D growth process is governed by the equilibrium between $NaO_{2(solv)}$ <--> $NaO_{2(solid)}$ and the mass transport of soluble product. By imaging the charge

process, we provide conclusive evidence that the same solvation-desolvation equilibrium is responsible for the dissolution of the NaO_2 discharge product, which consumes the NaO_2 cubes from the NaO_2-electrolyte interface towards the electrode and not from the cube-electrode interface. Therefore, we rule out the direct charge-transfer reaction as the major oxidation path for NaO_2 cubes and clarify the mechanism of this widely discussed reaction. Finally, we provide fundamental insights into the parasitic reactions occurring during cycling of a Na-O_2 battery where time-resolved visualization revealed the chemical reactivity of NaO_2 at the interface with the electrolyte. As a result, parasitic products continuously accumulate on the cube surface to form a thick shell surrounding the NaO_2 cubes, which passivates the electrode surface as it cannot be reoxidized. This information is vital for optimization of the battery, since this parasitic shell is responsible for the low efficiency during charge, as well as for its poor cyclability by preventing crucial O_2 redox and further nucleation of NaO_2. It must therefore be recognized that the NaO_2 growth is solvent dependent, providing the possibility of mediating the deposition process by controlling the solvation/desolvation event. Hence, caution must be exercised prior to generalizing this finding. Through this first visualization of the redox processes governing the Na-O_2 system, we further confirm the importance of finding how the various components of the batteries locally interact with each other. We hope these results will help in the development of new strategies to optimize cell components, such as the electrolyte, in order to achieve high performing Na-O_2 batteries, and also serve to motivate the development of *operando* electrochemical TEM cells.

Methods

Electrolyte preparation:

1,2-Dimethoxyethane (DME, 99.9%) was purchased from Sigma Aldrich and ($NaPF_6$ 99.9 %) was bought from Stella Chemifa. Solvents were dried by means of molecular sieves for 5 days

to remove excess water and Sodium salts were dried under vacuum at 80°C for 24 hours. The 0.5 M electrolyte solutions were prepared in an argon-filled glove box (0.1 ppm O_2/0.1 ppm H_2O). The water content of the electrolyte solutions was analyzed by Karl Fischer titration and was found to be below 20 ppm. The electrolyte was saturated with ultrapure O_2, prior to use in the *in situ* TEM cell.

***Operando electrochemical (S)TEM experiments**:*

Operando TEM experiments were performed using a FEI-TECNAI G2 (S)TEM equipped with a Schottky field-emission gun and an fast camera Oneview-Gatan (30 fps at 4k). For these experiments the microscope was operated at 200 kV in both conventional TEM and HAADF-STEM modes. In this study, we checked the effect of the electron beam used to make the observations in TEM and STEM modes to be sure that the beam does not have any effect on our results. During the observations, the dose was kept below 10 e^-/nm^2s in order to limit beam damage effects. By this way, typical beam effects (bubble and precipitate formations) due to the degradation of the electrolyte by radiolysis effect are avoided. As shown in Supplementary Figure S3, the insignificant impact of the electron beam on the liquid electrolyte was verified with the same dose of electron used during the fast imaging acquisition, which shows a high stability of $NaPF_6$/DME/O_2 electrolyte upon electron beam irradiation for a relatively long period of time: 360s. The TEM holder used is a Protochips Poseidon 510 owing both a microfluidic flow system and an electrochemical measurement system with 3 electrodes. The micro-battery cell itself is localized in the holder tip and consists of two silicon Echips sealed by Viton O-ring gasket: a top Echip (with 2 Pt electrodes (reference and counter) and 1 glassy carbon electrodes (working), a 500 nm SU-8 polymer spacer and a 50 nm thick Si_3N_4 window) and bottom Echip (with a 500 nm spacer and a 50 nm thick Si_3N_4 window). Mounted Echips are then compressed onto O-rings using screwed lid of the holder inducing a good vacuum-sealing. The microfluidic system integrated in the TEM holder allows to introduce and flow the electrolyte with a rate range from 0.5 to 5 µL/min. using a syringe pump system. The microfluidic system (cell and microtubes) is flushed by argon gas to discard oxygen presence prior to start *operando* experiment.

Cyclic voltammetry

CV experiments were conducted using an ultra low current SP-200 Biologic potentiostat, where during battery cycling, the potential was scanned at a rate of 10 mV/s between -1.6V and -3 V using Pt as pseudo-reference electrode and Pt as counter electrode. For sake of clarity, all values were then rescaled versus Na^+/Na to yield a potential window of 1.5 and 2.9V (vs. Na^+/Na).

X-ray photoelectron spectroscopy (XPS) analysis:

XPS analysis of the surface of aged sodium samples was performed by a means of SPECS Sage HR 100 spectrometer with a non-monochromatic X-ray source (Aluminum Kα line of 1486.6 eV energy and 300 W). The samples were placed perpendicular to the analyzer axis and calibrated using the $3d_{5/2}$ line of Ag with a full width at half maximum (FWHM) of 1.1 eV. All samples were transferred by means of a gastight transfer chamber to avoid air contact. All samples were further rinsed with dry DME solution to remove excess salt. In the case of sodium aged in TFSi electrolyte, the surface of the sample and not the precipitate was analyzed.

The selected resolution for the spectra was 10 eV of Pass Energy and 0.15 eV/step. All Measurements were made in an ultra-high vacuum (UHV) chamber at a pressure around $5 \cdot 10^{-8}$ mbar. An electron flood gun was used to compensate for charging during XPS data acquisition. In the fittings asymmetric and Gaussian-Lorentzian functions were used (after a Shirley background correction) where the FWHM of all the peaks were constrained while the peak positions and areas were set free. For every anion, XPS was performed on the surface of the metallic sodium. For TFSI, the XPS spectrum was collected as well on the surface of the metallic sodium, while the pilled off part wasn't analyzed.

Mass Spectrometry analysis:

The collected electrodes were first immersed in an aqueous solution containing 2M H_3PO_4, which decomposes Na_2CO_3 into CO_2. Due to the very acidic pH-value, the $2H^+ + CO_3^{2-} \leftrightarrow HCO^- + H^+ \leftrightarrow CO_2 + H_2O$ equilibrium is fully shifted to the right, where CO_2 evolves as gaseous CO_2, which is subsequently sampled by mass spectrometry. In a second step, after the CO_2 evolution has ended and all inorganic Na_2CO_3 was quantify, a second injection with 0.5 ml of a 2M H_3PO_4 solution containing 0.5M $FeSO_4$ and 40µL of 30% H_2O_2 (Fenton's

reagent) was added. The presence of the highly reactive $OH^{\bullet}$ radical (based on the Fenton`s reaction: $Fe^{2+} + H_2O_2 \rightarrow Fe^{3+} + OH^{\bullet} + OH^-$) leads to the decomposition of organic species (e.g.: sodium carboxylates) into CO_2, again released as gas due to the acidic environment.

Author contributions

A.G., A.D. and J.-M.T. designed the experiments. L.L., W.D., A.D. and A.G. performed the operando TEM measurements. W.D. and A.D. performed the TEM analysis. L.L., A.G., A.D. and J.-M.T. wrote the manuscript that all the authors edited.

Supporting Information Available:

Supplementary videos of *in situ* (S)TEM experiments, Cyclovoltammogram, XPS analysis, beam damage control experiments, EELS spectra, STEM-HAADF image, HAADF-STEM and EDX-STEM images of NaO_2 cubes grown on GDL electrodes.

Competing interests

The authors declare no competing financial interest.

Acknowledgements

L.Lutz thanks the ALISTORE-ERI for his Ph.D. grant. We would like to thank Dr. Artem Abakumov for fruitful discussions and comments on the manuscript.

References

1. Gallagher, K. G.; Goebel, S.; Greszler, T.; Mathias, M.; Oelerich, W.; Eroglu, D.; Srinivasan, V. *Energy & Environmental Science* **2014,** 7, 1555-1563.
2. Bruce, P. G.; Freunberger, S. A.; Hardwick, L. J.; Tarascon, J. M. *Nature Materials* **2012,** 11, 19–29.
3. Abraham, K. M.; Jiang, Z. *J. Electrochem. Soc.* **1996,** 143, 1-5.
4. Lepoivre, F.; Grimaud, A.; Larcher, D.; Tarascon, J.-M. *J. Electrochem. Soc.* **2016,** 163, A923-A929.
5. McCloskey, B. D.; Garcia, J. M.; Luntz, A. C. *J. Phys. Chem. Lett.* **2014,** 5, 1230-1235.

6. Ottakam Thotiyl, M. M.; Freunberger, S. A.; Peng, Z.; Chen, Y.; Liu, Z.; Bruce, P. G. *Nat Mater* **2013,** 12, 1050-1056.
7. Adelhelm, P.; Hartmann, P.; Bender, C. L.; Busche, M.; Eufinger, C.; Janek, J. *Beilstein J. Nanotechnol.* **2015,** 6, 1016-1055.
8. Liu, T.; Kim, G.; Casford, M. T. L.; Grey, C. P. *J. Phys. Chem. Lett.* **2016,** 7, 4841−4846.
9. Bender, C. L.; Hartmann, P.; Vracar, M.; Adelhelm, P.; Janek, J. *Adv. Energy Mater.* **2014,** 4, 1301863.
10. Kim, J.; Park, H.; Lee, B.; Seong, W. M.; Lim, H. D.; Bae, Y.; Kim, H.; Kim, W. K.; Ryu, K. H.; Kang, K. *Nat. Commun.* **2016,** 7, 10670-10679.
11. Knudsen, K. B.; Nichols, J. E.; Vegge, T.; Luntz, A. C.; McCloskey, B. D.; Hjelm, J. *J. Phys. Chem. C.* **2016,** 120, 10799–10805.
12. Morasch, R.; Kwabi, D. G.; Tulodziecki, M.; Risch, M.; Zhang, S.; Shao-Horn, Y. *ACS Appl. Mater. Interfaces* **2017,** 9, 4374-4381.
13. Lee, B.; Kim, J.; Yoon, G.; Lim, H.-D.; Choi, I.-S.; Kang, K. *Chem. Mater* **2015,** 27, 8406-8413.
14. Hartmann, P.; Bender, C. L.; Sann, J.; Duerr, A. K.; Jansen, M.; Janek, J.; Adelhelm, P. *Phys. Chem. Chem. Phys.* **2013,** 15, 11661-11672.
15. Hartmann, P.; Heinemann, M.; Bender, C. L.; Graf, K.; Baumann, R.-P.; Adelhelm, P.; Heiliger, C.; Janek, J. *J. Phys. Chem. C.* **2015,** 119, 22778-22786.
16. Yang, S.; Siegel, D. J. *Chem. Mater* **2015,** 27, 3852-3860.
17. Xia, C.; Black, R.; Fernandes, R.; Adams, B.; Nazar, L. F. *Nat. Chem* **2015,** 7, 496-501.
18. Pinedo, R.; Weber, D. A.; Bergner, B.; Schröder, D.; Adelhelm, P.; Janek, J. *J. Phys. Chem. C.* **2016,** 120, 8472-8481.
19. Ortiz-Vitoriano, N.; Batcho, T. P.; Kwabi, D. G.; Han, B.; Pour, N.; Yao, K. P.; Thompson, C. V.; Shao-Horn, Y. *J. Phys. Chem. Lett.* **2015,** 6, 2636-2643.
20. Das, S. K.; Xu, S.; Archer, L. A. *Electrochem. Commun.* **2013,** 27, 59-62.
21. Roberts, J. L. J.; Calderwood, T. S.; Sawyer, D. T. *J. Am. Chem. Soc.* **1984,** 106, 4667-4670.
22. Sayed, S. Y.; Yao, K. P.; Kwabi, D. G.; Batcho, T. P.; Amanchukwu, C. V.; Feng, S.; Thompson, C. V.; Shao-Horn, Y. *Chem Commun (Camb)* **2016,** 52, 9691-9694.
23. Black, R.; Shyamsunder, A.; Adeli, P.; Kundu, D.; Murphy, G. K.; F., N. L. *ChemSusChem* **2016,** 9, 1795 - 1803.
24. Landa-Medrano, I.; Pinedo, R.; Bi, X.; Ruiz de Larramendi, I.; Lezama, L.; Janek, J.; Amine, K.; Lu, J.; Rojo, T. *ACS Appl Mater. Interfaces* **2016,** 8, 20120–20127.
25. Reeve, Z. E.; Franko, C. J.; Harris, K. J.; Yadegari, H.; Sun, X.; Goward, G. R. *J. Am. Chem. Soc.* **2017,** 139, 595-598.
26. Liang, Z.; Zou, Q.; Wang, Y.; Lu, Y.-C. *Small Methods* **2017,** 1, 1700150.
27. Ross, F. M. *Science* **2015,** 350, aaa9886–aaa9886.
28. Dachraoui, W.; Kurkulina, O.; Hadermann, J.; Demortière, A. *Microsc. Microanal.* **2016,** 22, 24-25.
29. Holtz, M. E.; Yu, Y.; Gunceler, D.; Gao, J.; Sundararaman, R.; Schwarz, K. A.; Arias, T. A.; Abruna, H. D.; Muller, D. A. *Nano Lett.* **2014,** 14, 1453-1459.
30. Mehdi, B. L.; Qian, J.; Nasybulin, E.; Park, C.; Welch, D. A.; Faller, R.; Mehta, H.; Henderson, W. A.; Xu, W.; Wang, C. M.; Evans, J. E.; Liu, J.; Zhang, J. G.; Mueller, K. T.; Browning, N. D. *Nano Lett.* **2015,** 15, 2168-2173.
31. Sacci, R. L.; Black, J. M.; Balke, N.; Dudney, N. J.; More, K. L.; Unocic, R. R. *Nano Lett.* **2015,** 15, 2011-2018.

32. Luo, L.; Liu, B.; Song, S.; Xu, W.; Zhang, J. G.; Wang, C. *Nat Nanotechnol.* **2017,** 12, 535-540.
33. Hartmann, P.; Bender, C. L.; Vracar, M.; Duerr, A. K.; Garsuch, A.; Janek, J.; Adelhelm, P. *Nat. Mater* **2013,** 12, 228-232.
34. Lutz, L.; Yin, W.; Grimaud, A.; Alves Dalla Corte, D.; Tang, M.; Johnson, L.; Azaceta, E.; Sarou-Kanian, V.; Naylor, A. J.; Hamad, S.; Anta, J. A.; Salager, E.; Tena-Zaera, R.; Bruce, P. G.; Tarascon, J. M. *J. Phys. Chem. C.* **2016,** 120, 20068-20076.
35. Ottakam Thotiyl, M. M.; Freunberger, S. A.; Peng, Z.; Bruce, P. G. *J. Am. Chem. Soc.* **2013,** 135, 494-500.
36. Wandt, J.; Jakes, P.; Granwehr, J.; Gasteiger, H. A.; Eichel, R. A. *Angew. Chem.* **2016,** 128, 7006-7009.
37. Mahne, N.; Schafzahl, B.; Leypold, C.; Leypold, M.; Grumm, S.; Leitgeb, A.; Strohmeier, G. A.; Wilkening, M.; Fontaine, O.; Kramer, D.; Slugovc, C.; Borisov, S. M.; Freunberger, S. A. *Nat. Energy* **2017,** 2, 1-9.
38. Schafzahl, L.; Mahne, N.; Schafzahl, B.; Wilkening, M.; Slugovc, C.; Borisov, S. M.; Freunberger, S. A. *Angew Chem Int Ed Engl* **2017**, 56, 15728-15732.

FOR TABLE OF CONTENTS ONLY